Marwan Mokhtar
Research Engineer
Laboratory for Energy and Nano Science (LENS),
Department of Mechanical Engineering,
Masdar Institute of Science and Technology,
Abu Dhabi 54224, UAE
e-mail: marwan.mukhtar@gmail.com

Steven A. Meyers
Research Engineer
Laboratory for Energy and Nano Science (LENS),
Department of Mechanical Engineering,
Masdar Institute of Science and Technology,
Abu Dhabi 54224, UAE

Peter R. Armstrong
Associate Professor
Laboratory for Energy and Nano Science (LENS),
Department of Mechanical Engineering,
Masdar Institute of Science and Technology,
Abu Dhabi 54224, UAE
e-mail: parmstrong@masdar.ac.ae

Matteo Chiesa
Associate Professor
Laboratory for Energy and Nano Science (LENS),
Department of Mechanical Engineering,
Masdar Institute of Science and Technology,
Abu Dhabi 54224, UAE
e-mail: mchiesa@masdar.ac.ae

Performance of a 100 kW_{th} Concentrated Solar Beam-Down Optical Experiment

An analysis of the beam down optical experiment (BDOE) performance with full concentration is presented. The analysis is based on radiation flux distribution data taken on Mar. 21st, 2011 using an optical-thermal flux measurement system. A hypothetical thermal receiver design is used in conjunction with the experimental data to determine the optimal receiver aperture size as a function of receiver losses and flux distribution. The overall output of the plant is calculated for various operating temperatures and three different control strategies namely, constant mass flow of the heat transfer fluid (HTF), constant outlet fluid temperature and real-time optimal outlet fluid temperature. It was found that the optimal receiver aperture size (radius) of the receiver ranged between (1.06 and 1.71 m) depending on temperature. The optical efficiency of the BDOE ranged from 32% to 37% as a daily average (average over the ten sunshine hours). The daily average mean flux density ranged between 9.422 kW/m^2 for the 1.71 m-receiver and 20.9 kW/m^2 for the 1.06 m-receiver. Depending on the control parameters and assuming an open receiver with solar absorptivity of 0.95 and longwave emissivity of 0.10. The average receiver efficiency varied from 71% at 300 °C down to 68% at 600 °C. The overall daily average thermal efficiency of the plant was between 28% and 24%, respectively for the aforementioned temperatures. The peak of useful power collected in the HTF was around 105 kW_{th} at 300 °C mean fluid temperature and 89 kW_{th} at 600 °C.
[DOI: 10.1115/1.4027576]

1 Introduction

Central receiver concentrated solar power plants promise higher energy conversion efficiency and consequently lower levelized energy cost (LEC) [1]. It is expected that 48% reduction in tower plant costs will come from technology research and development [2]. The beam down concept provides the opportunity of locating bulky receivers on ground level in addition to the use of smaller receiver apertures and a final concentrating stage, which is made possible by the narrower view angle of concentrated radiation [3].

In order to demonstrate the potential of such configuration and investigate the possibility of a scale-up, a pilot 100 kW_{th} BDOE was constructed in 2009 in Masdar City Abu Dhabi (24.442°N 54.617°E), see Fig. 1.

The heliostat field consists of 33 ganged-type heliostats of totaling 280.5 m^2 of reflective area [4]. In this paper, we present optical and thermal performance analysis of the BDOE based on experimental data collected in Mar. 2011.

Optical performance is quantified by the optical efficiency, which includes the effects of cosine loss, reflexion loss, beam attenuation loss, blocking, and shading loss in addition to light spillage around central reflector (CR) mirrors and around the receiver aperture (intercept factor).The combined effect of the aforementioned (except for the final intercept factor) is evaluated experimentally using the flux measurement system. The intercept factor is a function of receiver aperture and flux distribution. Consequently, the receiver aperture size must be specified in order to evaluate the optical efficiency.

Thermal performance depends on the thermal efficiency of the receiver, which is also a function of receiver aperture size/geometry. Thermal performance depends additionally on the receiver operating temperature.

Due to the inverse relationship of receiver size to optical and thermal efficiency, it is necessary to conduct an optimization, which is based on operating temperature and maximum daily energy collection.

2 Experimental Setup

2.1 Heliostat Field. The BDOE heliostat field is designed for research convenience, not to be implemented on the utility scale. The heliostats are arranged in three concentric rings designated by letters with the closest ring called ring (A) and the furthest one (C) as depicted in Fig. 2. The numbers attached to these letters on the drawing increase in an anticlockwise manner with respect to the south of the field (pointing toward the top of the page). Note that four heliostats are missing from the each sector, one from the A-ring and three from the C-ring. This explains why there are 45 rather than 33 secondary mirrors on the CR.

Each heliostat is comprised of 43 flat facets—canted at different angles to create a Fresnel reflector such that the rays incident on the center of each facet will intersect (were the central reflectors absent) at the upper focal point of the CR. The area per heliostat is 8.5 m^2 yielding a total flat heliostat mirror area of 280.5 m^2 for the entire field. These unconventional heliostats allow for a better utilization of land space and a more compact system design compared to conventional heliostats (see Fig. 1(*a*)).

2.2 Central Reflector. The central tower is 16.0 m in height, supporting 45 fixed, flat CR mirrors. Each of the 33 CR mirrors currently in use reflects the converging rays from one heliostat back down onto the target (Table 1).

The CR mirrors are arranged in concentric circles corresponding to the heliostat rings. The mirrors in each ring are tilted with respect to the normal of the target by the same angle, creating a hyperboloidal Fresnel reflector. The innermost ring corresponds to the heliostats' A-ring, and has the smallest tilt angle of the three,

Contributed by the Solar Energy Division of ASME for publication in the JOURNAL OF SOLAR ENERGY ENGINEERING: INCLUDING WIND ENERGY AND BUILDING ENERGY CONSERVATION. Manuscript received April 7, 2014; final manuscript received April 10, 2014; published online May 15, 2014. Editor: Gilles Flamant.

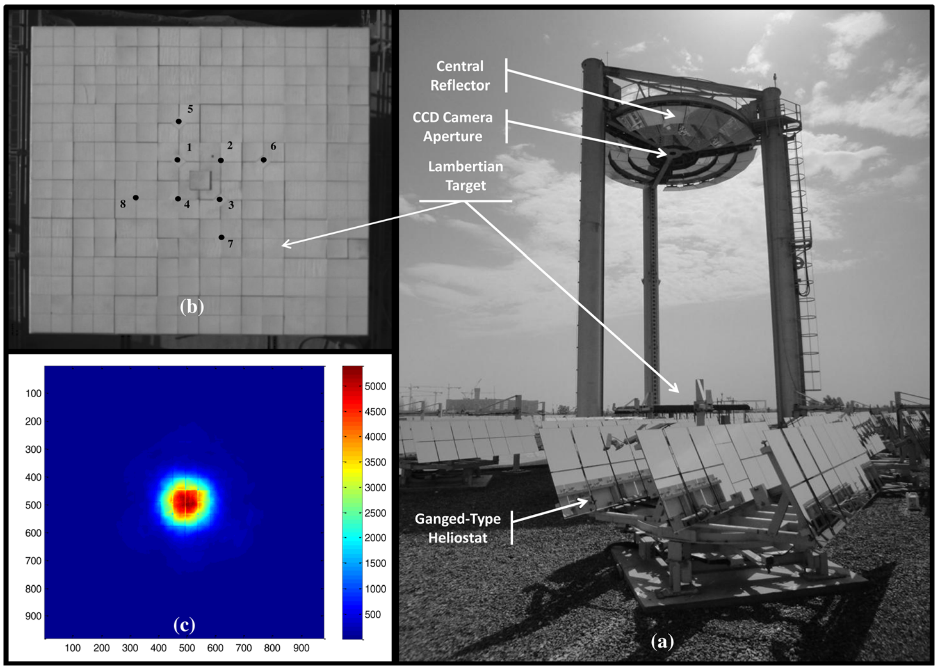

Fig. 1 BDOE overview. (*a*) Ganged-Type heliostat field and CR mirrors. CCD camera aperture is in the center of the CR taking images of the target below it. (*b*) Embedded within the target are water-cooled HFS at eight locations to calibrate the CCD camera images. (*c*) A typical luminance map taken by the CCD camera.

whereas the ring located furthermost from the center of the tower corresponds to the C-ring heliostats (Fig. 2).

The CR mirrors in the BDOE plant are exposed to about 10 suns. Use of a multifaceted CR reduces temperature related mechanical stress and improves natural cooling, thus avoiding the thermal stress problem. In addition, using separate reflectors as opposed to a continuous monolithic hyperboloid surface reduces manufacturing, shipping, and erection costs.

2.3 Measurement System. To study energy flux distribution and its magnitude on the receiver plane of the BDOE, the concentrated solar radiation is intercepted by a 5 m $\times$ 5 m ceramic tile target, located 2.3 m above ground level (see Fig. 1). These white tiles can withstand the high flux levels and are highly reflective in a diffuse manner approximating a Lambertian target. This allows a CCD camera located at the top of the tower to measure the distribution of luminous intensity. Embedded within the tiles at eight locations are heat flux sensors (HFS) to measure the concentrated solar flux. The HFSs only provide discrete thermal flux data and the CCD camera provides data of the luminous intensity on the target. A correlation was developed between the flux sensor data and the CCD camera data so that an accurate measurement of flux distribution can be obtained. In this way enough information of flux distribution on the focal plane can be acquired at each moment of time which allows the study of the BDOE performance under various conditions.

The CCD camera temperature is controlled by a combination of heating and cooling devices. A proportional integral differential controller regulates the air pressure supplied to a vortex cooler in order to keep the CCD camera temperature constant at 23 °C.

Table 1 Summary of BDOE parameters

Item	Value
Nominal power	100.0 kW_{th}
Number of heliostats	33
Reflective area per heliostat	8.5 m^2
Primary reflective area	280.5 m^2
CR mirrors reflectivity	95%
Heliostats mirrors reflectivity	80%
Upper focal point	20.0 m
Lower focal point	2.0 m
CR height	16.0 m
CR ring A diameter	3.5 m
CR ring B diameter	5.4 m
CR ring C diameter	7.4 m
Heliostat ring A diameter	17.48 m
Heliostat ring B diameter	27.08 m
Heliostat ring C diameter	36.68 m

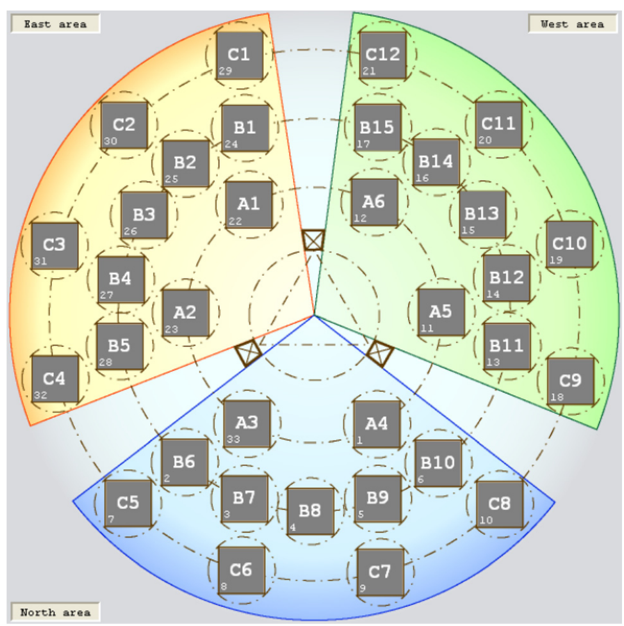

Fig. 2 BDOE heliostat field

The heat flux sensors used in the measurement system also require cooling. For accurate heat flux measurement, it is more important to prevent transients in water temperature than to keep a precise set point. Cooling water is supplied from a tank of sufficient thermal mass to prevent any abrupt change in the water temperature and to operate for several hours with less than 20 K temperature rise. The water temperature going into the sensors and the outlet temperature of each sensor are recorded and then used in correcting the HFS for thermal losses using a correction model developed in Ref. [5].

The foregoing combinations of optical and thermal radiometry provide the required flux maps. While heat flux measurement is accurate and reliable, it is only feasible to be implemented at discrete points on the target. Optical methods on the other hand are less accurate but provide very high spatial resolution. Heat flux measurement is used as a reference for calibrating the optical system and hence combining the advantages of the two methods. Similar hybrid measurement systems have been used to measure heat flux on the targets of parabolic dishes [6] and tower plants [7,8].

3 Performance Analysis

In this section, we present the method used for analyzing the performance of the BDOE. The optical performance of the plant (not including the intercept factor) is evaluated from the experimental results acquired by a flux measurement system. Then, the intercept factor and the receiver thermal performance are evaluated simultaneously for varying operating temperatures using the aperture size optimization algorithm which is described later in Sec. 3.2.

3.1 Receiver Thermal Performance. Heat loss from solar receivers is a subject of much literature. McDonald [9] presented a comprehensive investigation of heat loss from cavity receivers including convection, radiation and conduction. Receiver convection loss has been studied in great detail by Clausing [10–12] and others [13–16]. These studies included analytical and numerical models supported by experimental studies for various geometries and receiver orientations. Most of these studies only considered losses from downward facing receivers, Leibfried and Ortjohann [13] also considered upward facing receivers.

Although some studies considered wind induced forced convection [17], most studies neglected forced convection loss from cavity receivers [10,13,14,16].

In this paper, we base our analysis on the performance of an upward facing open receiver and neglect forced convection effects because the mean wind speed during the test was small (2.6 m/s).

Here, we present the equations and procedure used in assessing the performance of a hypothetical receiver. The method is based on the Hottel-Whillier equation [18] as presented in Duffie and Beckman [19]. The HTF selected for the analysis is liquid sodium. Under steady state conditions the net useful power output of the receiver is the difference between the absorbed solar radiation and the thermal loss from the receiver surface.

$$\dot{Q}_u = A(\alpha \dot{q}_{\mathrm{in}} - U_L(T_{\mathrm{mp}} - T_e)) \tag{1}$$

where $\dot{Q}_u$ is the useful heat output, α is the absorptivity of the receiver in the solar spectrum (taken as 95%), $\dot{Q}_{\mathrm{in}}$ is the solar power intercepted by the receiver aperture, A, U_L is the overall heat loss coefficient, T_{mp} is the mean plate temperature, and T_e is the air temperature both in K.

Equation (1) is reformulated in terms of the inlet fluid temperature (T_{fi}) and the heat removal factor (F_R). F_R is introduced to account for the underestimated losses calculated based on the inlet fluid temperature (T_{fi}) instead of mean plate temperature.

$$\dot{Q}_u = AF_R(\alpha \dot{q}_{\mathrm{in}} - U_L(T_{\mathrm{fi}} - T_e)) \tag{2}$$

The heat removal factor F_R is the ratio of useful gain to what it would have been had the whole absorber plate been at the inlet fluid temperature [19]. F_R is given by

$$F_R = \frac{\dot{m}c_p}{AU_L}\left(1 - e^{-\frac{AU_L F'}{\dot{m}C_p}}\right) \tag{3}$$

where $\dot{m}$ is the mass flow rate, C_p is the specific heat of HTF, and F' is the receiver plate efficiency factor [19] that accounts for the thermal resistance between the plate and the fluid inside the tubes

$$F' = \frac{1}{U_L D_O\left(\frac{1}{U_L D_i} + \frac{1}{\pi D_i h_f}\right)} \tag{4}$$

where D_o is the outer tube diameter, D_i is the inner tube diameter, and h_f is the convection heat transfer coefficient between the inner wall and the fluid given by

$$h_f = \frac{\mathrm{Nu}_f k_f}{D_i} \tag{5}$$

For liquid metals like liquid sodium, a convection heat transfer correlation between the fluid and the tube walls is given by [20]

$$\begin{aligned} \mathrm{Nu}_f &= 6.3 + 0.0167 R_e^{0.85} \mathrm{Pr}^{0.93} \quad \text{Turbulent} \\ \mathrm{Nu}_f &= 4.36 \quad \text{Laminar} \end{aligned} \tag{6}$$

where Pr is the Prandtl number, which is the ratio between kinematic viscosity and thermal diffusivity $\mathrm{Pr} = \nu/\alpha$, and Re is the Reynolds number which represents the ratio between inertial and viscous forces $\mathrm{Re} = vD/\nu$.

The overall heat loss coefficient U_L accounts for all heat losses from the receiver. There are five main loss mechanisms associated with the receiver of a concentrated solar plant: convective loss, radiative loss, conductive loss, loss due to reflection, and spillage. Conductive heat losses are assumed to be negligible compared to other loss mechanisms, while losses due to spillage are accounted for in the calculation of radiant power intercepted by the receiver (Sec. 3.2). Reflective losses and spillage around the CR are accounted for by the fact that radiation is measured at receiver aperture level.

According to Ref. [21], in a well designed receiver, thermal losses account for 5–15% of incident, hence a reasonable estimate using T_{mp} is adequate to determine receiver performance.

We assume, as mentioned earlier, that the dominant convection mode is free convection and that forced convection is negligible. The aperture Nusselt number for laminar and turbulent flows are given by [20]

$$\begin{aligned} \overline{\mathrm{Nu}}_{\mathrm{natural}} &= 0.54(\mathrm{Gr}_L \mathrm{Pr})^{1/4} \quad \text{Turbulent} \\ \overline{\mathrm{Nu}}_{\mathrm{natural}} &= 0.14(\mathrm{Gr}_L \mathrm{Pr})^{1/3} \quad \text{Laminar} \end{aligned} \tag{7}$$

where Grashof number for free convection is given by [20]

$$\mathrm{Gr}_L = \frac{\beta \Delta T g L^3}{\nu^2} \tag{8}$$

where β is the volumetric thermal expansion coefficient in K^{-1}, ΔT is the temperature difference between mean plate temperature (T_{mp}), and ambient air temperature (T_e) in K, g is the gravitational acceleration in m/s^2, $L = 2R$ is the characteristic length of the receiver equal to its diameter in m, and ν is the kinematic viscosity of air in m^2/s.

Hence the convection heat transfer coefficient (in W/m^{2}K) is given by

$$\bar{h}_c = \frac{k\mathrm{Nu}}{L} \tag{9}$$

where k is the is the conductivity of air in W/mK and $L = 2R$ is again the aperture diameter in m.

The temperature dependence of fluid properties was taken into account during calculations.

The radiative heat loss is given by

$$\dot{Q}_{\mathrm{rad}} = A\varepsilon\sigma(T_{\mathrm{mp}}^4 - T_{\mathrm{sky}}^4) \tag{10}$$

where $\dot{Q}_{\mathrm{rad}}$ is the radiative heat loss in W, ε is the longwave emissivity (taken as 10% assuming selectivity to reduce radiative losses. The selectivity mechanism is assumed to remain stable across the operating temperature range), T_{mp} is the mean plate temperature and T_{sky} is the effective sky temperature both in K. A pyrgeometer was used to measure effective sky temperature during the experiment. Hence, the linearized radiative heat transfer coefficient relative to air temperature may be defined as

$$\bar{h}_r = A\varepsilon\sigma\frac{T_{\mathrm{mp}}^4 - T_{\mathrm{sky}}^4}{T_{\mathrm{mp}} - T_e} \tag{11}$$

The mean plate temperature T_{mp} required for solving the previous equations can be calculated by

$$T_{\mathrm{mp}} = T_{\mathrm{fi}} + \frac{Q_u}{AF_R U_L}(1 - F_R) \tag{12}$$

Finally, the overall heat loss coefficient is given by

$$U_L = \bar{h}_r + \bar{h}_c \tag{13}$$

3.2 Receiver Intercept Factor. The power intercepted by the receiver will depend on the receiver aperture size. Spillage is caused by various optical and mechanical errors in the concentration system, in addition to the effect of sunshape on beam widening. Fig. 3 depicts the day-average intercept factor variation with receiver aperture radius. The receiver intercept factor γ is calculated as follows:

$$\gamma = \frac{\int_0^R \int_0^{2\pi} G(r,\theta)d\theta dr}{\int_0^\infty \int_0^{2\pi} G(r,\theta)d\theta dr} \tag{14}$$

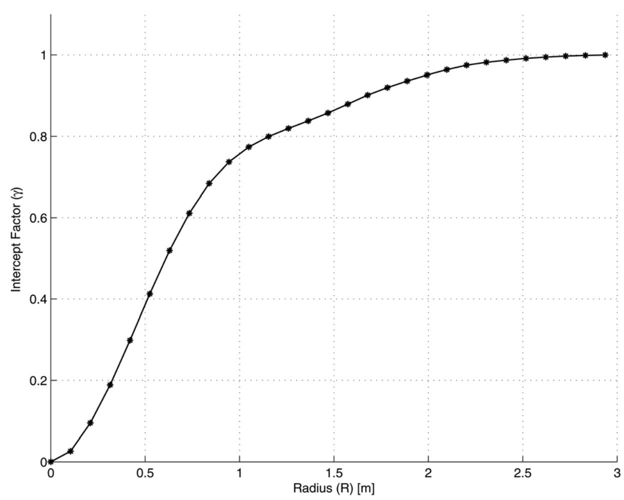

Fig. 3 Day-average intercept factor (γ) as a function of receiver aperture radius (R)

where R is the receiver intercept factor, R is the receiver aperture radius, and $G(r, \theta)$ is the flux map defined in polar coordinates.

3.3 Receiver Aperture Sizing. Optimal receiver aperture size is determined by maximizing the day average useful power in Eqn. 2. This is calculated based on the required outlet mean fluid temperature. An iterative algorithm is used for evaluating the receiver performance and finding the optimal receiver size. Depending on the temperature/flow control strategy used, the algorithm is slightly modified. The main calculation steps are:

(1) Calculation of cumulative radial flux distributions which give the relation between receiver size (R) and intercepted power (Q_{in}).
(2) Specification of control strategy and setpoint of control variable: mass flow, outlet temperature or optimal outlet temperature.
(3) Selection of a receiver radius (R).
(4) Calculation of receiver performance based on input parameters: T_{fi}, T_{fo}, R, Q_{in}, and ambient conditions.
  (a) Radiation and convection heat transfer coefficients ($\bar{h}_r, \bar{h}_c$) are calculated using an initial value for the mass flow rate ($\dot{m}$) and mean plate temperature (T_{mp}).
  (b) Receiver efficiency factor (F') is calculated.
  (c) $\dot{m}$ is updated using the calculated (F') and overall heat loss coefficient (U_L).
  (d) Net useful power (Q_u) is updated using the new $\dot{m}$, where $Q_u = \dot{m}c_p(T_{\mathrm{fo}} - T_{\mathrm{fi}})$.
  (e) Heat removal factor (F_R)is updated with the new Q_u.
  (f) T_{mp} is updated.
  (g) Steps a-f are repeated until T_{mp} is accurate enough.

(5) The calculation (4) is repeated for different R and T_{fo}.

4 Results

In this section, we present the results obtained from the evaluation of BDOE performance under full concentration using the experimental data collected and the receiver model we presented in Sec. 3.3. Direct normal irradiation (DNI) during the test day is shown in Fig. 4.

4.1 Optical Efficiency. Figure 5 depicts the optical efficiency calculated based on the optimal receiver size chosen for each fluid outlet temperature. Optical efficiency represents the amount of energy that is intercepted by the receiver aperture normalized by the product of incident DNI and heliostat area. Optical efficiency accounts for all the factors that reduces the amount of concentrated radiation until it reaches the receiver, but before it gets converted into thermal power. Optical efficiency includes cosine

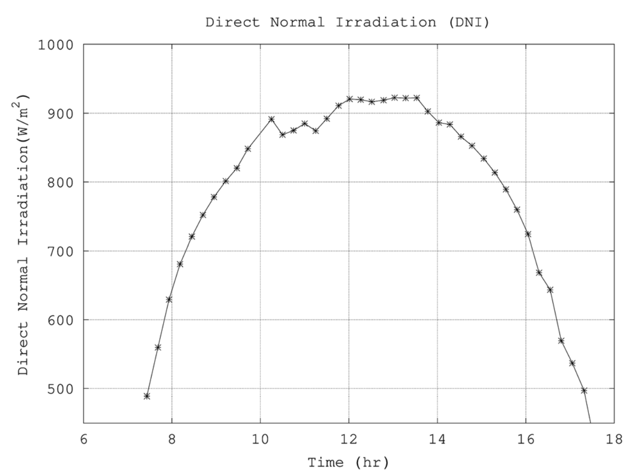

Fig. 4 DNI during the test day

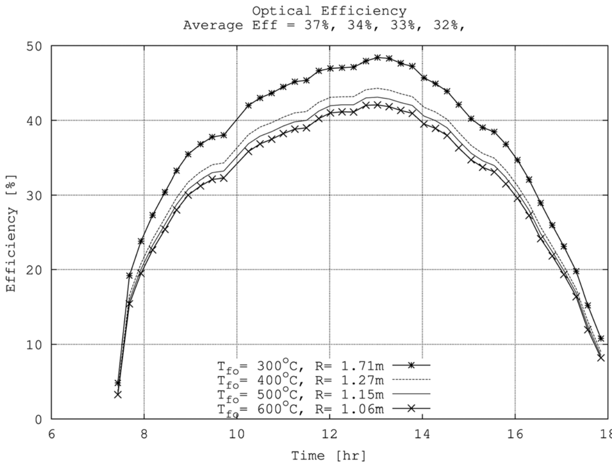

Fig. 5 Optical efficiency with optimal aperture

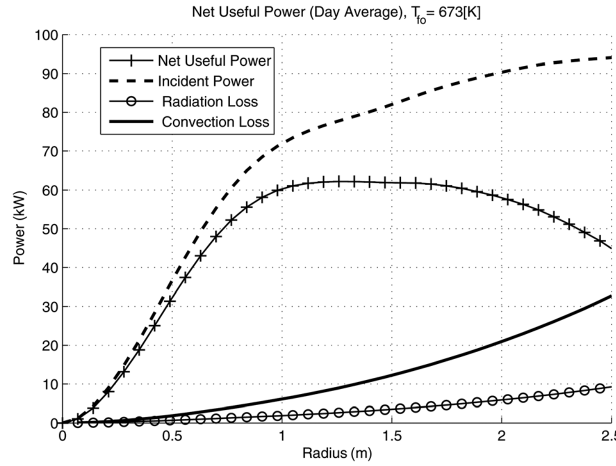

Fig. 8 Net power collected as a function of receiver radius. Convection and radiation losses are also shown as a function of receiver size, $T_{fo} = 400\,^{\circ}$C. Daily average is calculated over the ten sunshine hours of the test day.

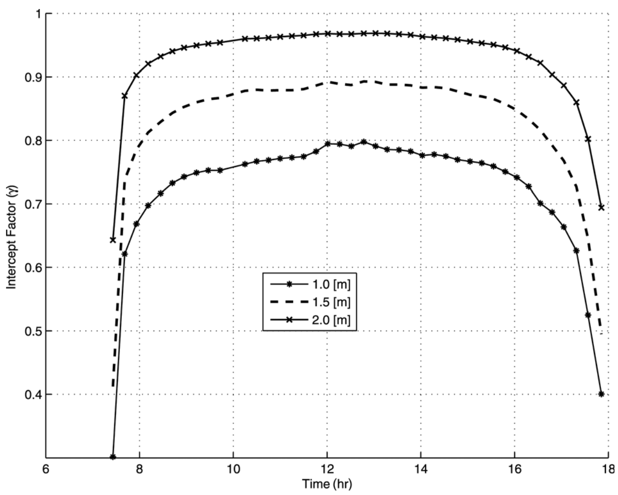

Fig. 6 Intercept factor variation during the test day for different receiver aperture sizes

factor, reflectivity of both heliostats and the CR mirrors, beam attenuation, CR intercept factor (spillage), incident angle modifier, blocking and shading of heliostats, and the intercept factor of the receiver.

The test was conducted after all heliostat and CR mirrors were cleaned. The reflectivities of representative mirror samples were measured in the lab and were spectrally weighted with a 1.5 air mass solar spectrum. This analysis yielded an 80% reflectivity for the heliostat mirrors and 95% for the CR mirrors. Under normal conditions however, mirrors were left to soil for several days and the reflectivity of the mirrors was degraded by dirt and sand, accounting for a considerable optical losses. In Fig. 5, it can be seen that the average efficiency of the receiver is varying with outlet temperature from 32% to 37%; this is because the optimal receiver size changes based on the specified outlet temperature. Since higher temperatures call for smaller receiver apertures, the optical efficiency is reduced directly by the lower intercept factor for smaller receiver radii.

Figure 6 depicts the daily variation of intercept factor for different receiver sizes based on the upper limit of integration, R, in 14. The drop in intercept factor on either side of solar noon stems mainly from the well-known effects of off-axis aberration (astigmatism) associated with heliostat optics (Fig. 7). The elongated flux distributions observed in morning and afternoon result in radiation spilling outside the receiver aperture [22].

4.2 Receiver Thermal Efficiency. Receiver thermal efficiency is a function of its mean temperature and incident flux per unit aperture size. Figure 8 illustrates as a function of aperture radius, the incident power on the receiver, convection losses, radiation losses, and net useful output. The curves are calculated for an outlet fluid temperature of 400 °C. It can be seen that a maximum for net power occurs at a certain receiver radius. Figure 9 depicts the daily variation of receiver thermal efficiency for several outlet fluid temperatures, and also indicates that the receiver thermal efficiency at 300 °C ($R = 1.71$ m) is less than that at 400 °C

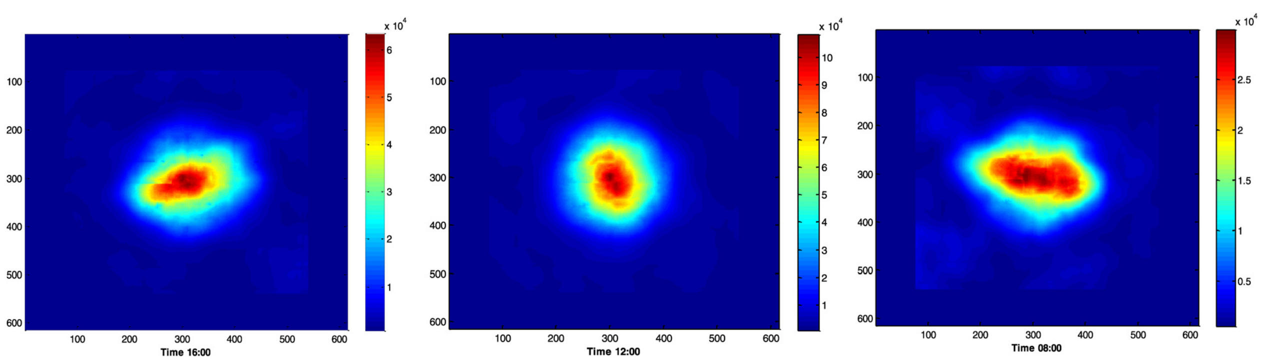

Fig. 7 Luminance maps at different times of the day (local time UTC+4) shown in cd/m². *x* and *y* axes are in pixels. Aberration is evident in early and late parts of the day which correspond to reduced intercept factor.

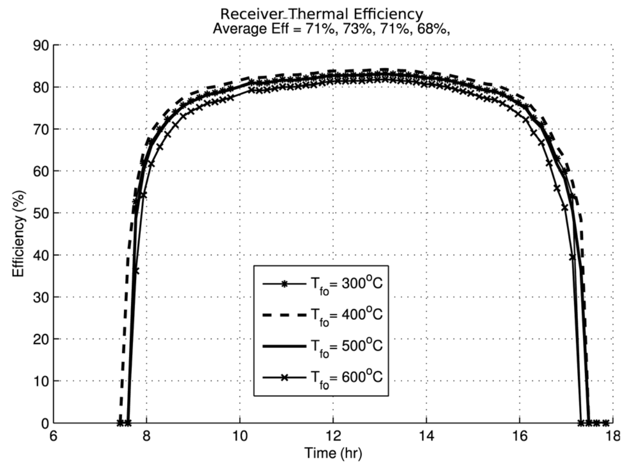

Fig. 9 Receiver thermal efficiency. Average efficiency at 300 °C is 71%, at 400 °C is 73%, at 500 °C is 71% and at 600 °C is 68%.

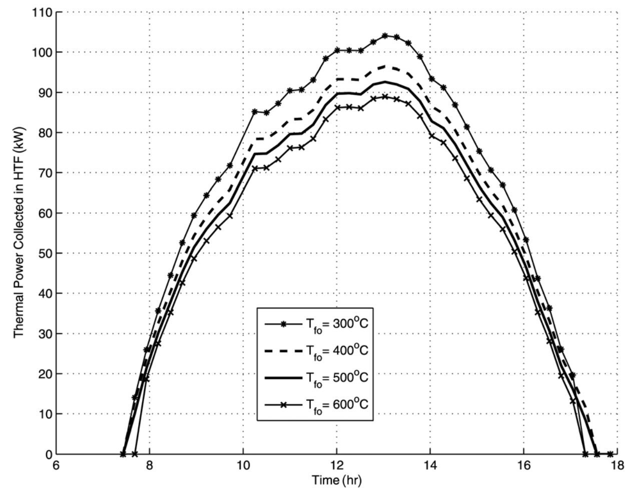

Fig. 11 Thermal output of the receiver as function of time and outlet temperature

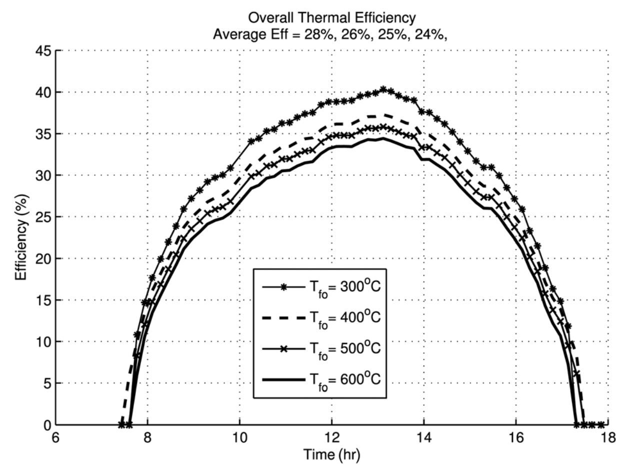

Fig. 10 Overall efficiency of the BDOE. Overall efficiency at 300 °C is 28%, at 400 °C is 26%, at 500 °C is 25%, and at 600 °*C* is 24%.

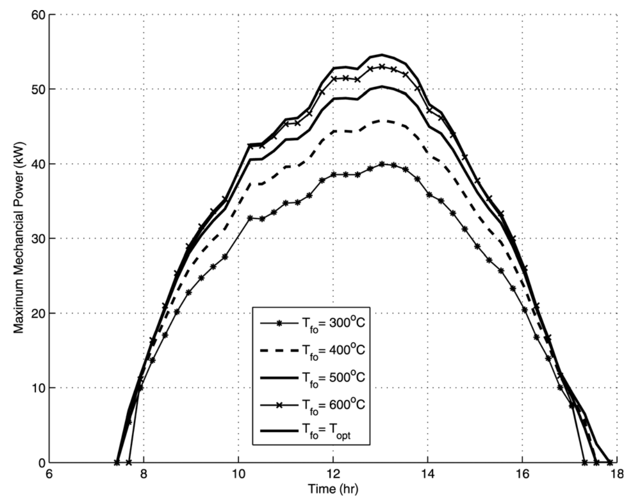

Fig. 12 Maximum mechanical power, which is indicative of the solar-to-electricity efficiency of the BDOE

($R = 1.27$ m). This is because the optimal receiver aperture size at 400 °C is larger, which resulted in a higher thermal loss despite the lower operating temperature. At higher temperatures the effect of thermal losses starts to dominate over the aperture size and we see that thermal efficiency becomes mainly a function of outlet temperature. It is important to note that since receiver aperture size is optimized for overall efficiency, the overall efficiency is higher at 400 °C than at the higher outlet temperatures will be shown in Sec. 4.3.

4.3 Overall Efficiency for Heat and Power Output. The overall efficiency (Fig. 10) is the product of optical and thermal efficiencies, as expected it is inversely proportional to the outlet temperature and varying on average from 22% to 26%. Figure 11 depicts the thermal power output (kW) collected in the HTF for different temperatures. The total energy varies from 623.1 kWh at 400 °C to 529.2 kWh at 700 °C.

Figure 12 depicts the maximum possible mechanical power (exergy rate) of the fluid for varying temperatures, calculated based on Carnot efficiency assuming cold reservoir temperature of 80 °C. Maximum possible mechanical power is also calculated for real-time optimized fluid outlet temperature ($T_{fo} = T_{opt}$). See Sec. 4.4.

4.4 Comparison of Control Strategies. The selection of the control strategy is often dictated by the consumer process, most processes require a constant temperature supply from the heat source. This obvious challenge for solar systems maybe overcome by some kind of thermal inertia (storage) or hybridization with fossil fuel based sources. Therefore, the solar engineer might have the choice between constant-temperature-variable-flow control strategy, constant-flow-variable-temperature control strategy or a variable-temperature-variable-flow control strategy that maximizes exergy (or other objective function).

While constant flow control is the easiest to implement practically because it requires less hardware and also simpler control, the merits of the other control strategies might justify the change, this has to be assessed on a system level. The objective function must be modified to include the consumer process operation parameters.

Figure 13 shows simulation results for the three aforementioned control strategies. It can be seen in (a) that the differences between the three control strategies is small. This is because the constant temperature and constant flow rate were also selected by maximizing the objective function.

If the temperature deviates from the optimized constant temperature then the mechanical power will be lower (see Fig. 12). It should be noted that although the optimal mass flow and outlet

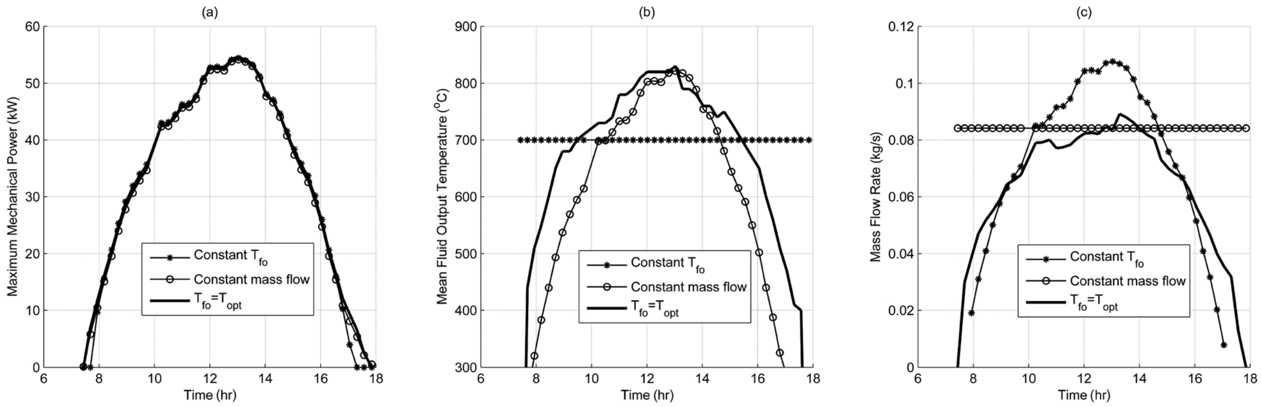

Fig. 13 Comparison of control strategies. (*a*) Daily variation of maximum mechanical power, (*b*) mean fluid output temperature, (*c*) mass flow rate.

temperature are constant in this example day, they are expected to change during the year. Moreover, the small differences among the control strategies are affected by receiver design, which, in this case, has low thermal losses. For less efficient receivers, the real time optimized temperature control strategy may have a significant advantage.

5 Conclusions

The overall efficiency of the BDOE is estimated to vary from 24% to 28% during the test day. The main losses in the system are optical losses: cosine loss, reflectivity loss, beam attenuation loss, blocking, and shading loss in addition to light spillage around CR mirrors and around the receiver aperture (intercept factor).

The optical efficiency of the system can be improved by better adjustment of the heliostats facet canting and also the canting of the CR mirrors to avoid spillage around the CR mirrors and the receiver, respectively.

The beam down optical arrangement suffers certain optical losses, mainly the CR spillage and reflection losses which are not incurred by a conventional tower receiver system. However, these losses may be outweighed by the potential to use a cavity type receiver and possibly a final compound parabolic concentrator optical element made possible by the relatively narrow angular distribution (maximum incident angle of 17 deg) of radiation incident on the receiver. Beam down plants have the additional advantage of locating the receiver at ground level to reduce installation and operational costs.

Nomenclature

A = receiver aperture area (m^2)
C_p = specific heat of the HTF(kJkg^{-1}K^{-1})
D_i = receiver tube inside diameter (m)
D_o = receiver tube outside diameter (m)
F' = receiver plate efficiency factor
F_R = heat removal factor
g = gravitational acceleration (m/s^2)
Gr = Grashof number
$G(r, \theta)$ = radiation flux map in polar coordinates (kW/m^2)
$\bar{h}_c$ = receiver convection heat loss coefficient (kWm^{-2}K^{-1})
h_f = convection heat transfer coefficient between HTF and tube wall (kWm^{-2}K^{-1})
$\bar{h}_r$ = receiver linearized radiative heat transfer coefficient (kWm^{-2}K^{-1})
k = thermal conductivity of air (Wm^{-1}K^{-1})
L = receiver characteristic length (m)
$\dot{m}$ = HTF mass flow rate (kg/s)
Nu = Nusselt number
Pr = Prandtl number
$\dot{q}_{in}$ = solar flux intercepted by the receiver (kW/m^2)
$\dot{Q}_{rad}$ = radiative heat loss (kW)
$\dot{Q}_u$ = useful thermal power (kW)
R = receiver aperture radius (m)
Re = Reynolds number
T_e = ambient air temperature (°C)
T_{fi} = inlet mean fluid temperature (°C)
T_{film} = mean film temperature (°C)
T_{fo} = outlet mean fluid temperature (°C)
T_{opt} = real-time optimized fluid outlet mean temperature (°C)
T_{mp} = mean plate temperature (°C)
T_{sky} = effective sky temperature (°C)
U_L = overall heat loss coefficient (kWm^{-2}K^{-1})
α = receiver absorptivity in solar spectrum
β = volumetric thermal expansion coefficient (K^{-1})
ΔT = temperature difference between mean plate temperature and ambient air temperature (K)
ε = receiver longwave emissivity
γ = receiver intercept factor
ν = kinematic viscosity of air (m^2/s)
σ = Stefan-Boltzmann constant (5.670373 $\times$ 10^{-8}Wm^{-2}K^{-4})

References

[1] Kaltschmitt, M., Streicher, W., and Wiese, A., 2007, *Renewable Energy: Technology, Economics and Environment*, Springer, New York.
[2] Charles, R. P., Smith, J. L., and Davis, K. W., 2003, "Assessment of Parabolic Trough and Power Tower Solar Technology Cost and Performance Forecasts," Sargent & Lundy LLC Consulting Group, National Renewable Energy Laboratory, Golden, CO.
[3] Tamaura, Y., Utamura, M., Kaneko, H., Hasuike, H., Domingo, M., and Relloso, S., 2006, "A Novel Beam-Down System for Solar Power Generation With Multi-Ring Central Reflectors and Molten Salt Thermal Storage," Proceedings of the 13th International Symposium on Concentrating Solar Power and Chemical Energy Technologies, Seville, Spain.
[4] Hasuike, H., Yuasa, M., Wada, H., Ezawa, K., Oku, K., Kawaguchi, T., Mori, N., Hamakawa, W., Kaneko, H., and Tamaura, Y., 2009, "Demonstration of Tokyo Tech Beam-Down Solar Concentration Power System in 100 kW Pilot Plant," Proceedings of 15th International Symposium on Concentrated Solar Power and Chemical Energy Technologies, Berlin, Germany.
[5] Mokhtar, M. M., Meyers, S. A., Rubalcaba, I., Chiesa, M., and Armstrong, P. R., 2012, "A Model for Improved Solar Irradiation Measurement at Low Flux," Sol. Energy, **86**(3), pp. 837–844.
[6] Ulmer, S., Reinalter, W., Heller, P., Lupfert, E., and Martinez, D., 2002, "Beam Characterization and Improvement With a Flux Mapping System for Dish Concentrators," ASME J. Sol. Energy Eng., **124**(2), pp. 182–188.
[7] Ballestrín, J., and Monterreal, R., 2004, "Hybrid Heat Flux Measurement System for Solar Central Receiver Evaluation," Energy, **29**(5–6), pp. 915–924.
[8] Ulmer, S., Lüpfert, E., Pfänder, M., and Buck, R., 2004, "Calibration Corrections of Solar Tower Flux Density Measurements," Energy, **29**(5–6), pp. 925–933.
[9] McDonald, C. G., 1995, "Heat Loss From an Open Cavity," Sandia National Laboratories, Technical Report SAND95-2939.
[10] Clausing, A., 1981, "An Analysis of Convective Losses From Cavity Solar Central Receivers," Sol. Energy, **27**(4), pp. 295–300.

[11] Clausing, A. M., 1983, "Natural Convection Correlations for Vertical Surfaces Including Influences of Variable Properties," ASME J. Heat Transfer, **105**(1), pp. 138–143.
[12] Clausing, A. M., Waldvogel, J. M., and Lister, L. D., 1987, "Natural Convection From Isothermal Cubical Cavities With a Variety of Side-Facing Apertures," ASME J. Heat Transfer, **109**(2), pp. 407–412.
[13] Leibfried, U., and Ortjohann, J., 1995, "Convective Heat Loss from Upward and Downward-Facing Cavity Solar Receivers: Measurements and Calculations," ASME J. Sol. Energy Eng., **117**(2), pp. 75–84.
[14] Taumoefolau, T., Paitoonsurikarn, S., Hughes, G., and Lovegrove, K., 2004, "Experimental Investigation of Natural Convection Heat Loss From a Model Solar Concentrator Cavity Receiver," ASME J. Sol. Energy Eng., **126**(2), pp. 801–807.
[15] Prakash, M., Kedare, S., and Nayak, J., 2009, "Investigations on Heat Losses From a Solar Cavity Receiver," Sol. Energy, **83**(2), pp. 157–170.
[16] Paitoonsurikarn, S., Lovegrove, K., Hughes, G., and Pye, J., 2011, "Numerical Investigation of Natural Convection Loss From Cavity Receivers in Solar Dish Applications," ASME J. Sol. Energy Eng., **133**(2), p. 021004.
[17] Ma, R. Y., 1993, "Wind Effects on Convective Heat Loss From a Cavity Receiver for a Parabolic Concentrating Solar Collector," Sandia National Laboratories, Technical Report SAND92-7293.
[18] Hottel, H., and Whillier, A., 1958, "Evaluation of Flat-Plate Solar Collector Performance," Transactions of the Conference on Use of Solar Energy, E. F. Carpenter, ed., University of Arizona Press, Tucson, AZ, p. 74.
[19] Duffie, J. A., and Beckman, W. A., 2006, *Solar Engineering of Thermal Processes*, 3rd ed., Wiley, New York.
[20] Mills, A. F., 1998, *Heat Transfer*, 2nd ed., Prentice Hall, Englewood Cliffs, NJ.
[21] Winter, C.-J., Sizmann, R. L., and Vant-Hull, L. L., 1991, *Solar Power Plants: Fundamentals, Technology, Systems, Economics*, 1st ed., Springer, New York.
[22] Mokhtar, M., Rubalcaba, I., Meyers, S., Qadir, A., Armstrong, P., and Chiesa, M., 2010, "Heliostat Field Efficiency Test of Beam-Down CSP Pilot Plant—Experimental Results," Proceedings of the 16th International Symposium on Concentrating Solar Power and Chemical Energy Technologies, Perpignan, France.